UC San Diego
UC San Diego Previously Published Works

Title
Assessment of ICESat-2 for the recovery of ocean topography

Permalink
https://escholarship.org/uc/item/18j4k8nz

Journal
Geophysical Journal International, 226(1)

ISSN
0956-540X

Authors
Yu, Yao
Sandwell, David T
Gille, Sarah T
et al.

Publication Date
2021-05-06

DOI
10.1093/gji/ggab084

Peer reviewed

Assessment of ICESat-2 for the Recovery of Ocean Topography

Yao Yu[1*], David T. Sandwell[1], Sarah T. Gille[1] and Ana Beatriz Villas Bôas[1]

[1]Scripps Institution of Oceanography, University of California San Diego, La Jolla, CA, USA

Corresponding author: Yao Yu (yayu@ucsd.edu)

Summary

The Ice, Cloud, and land Elevation Satellite 2 (ICESat-2) laser altimetry mission, launched in September 2018, uses 6 parallel lidar tracks with very fine along-track resolution (15 m) to measure the topography of ice, land, and ocean surfaces. Here we assess the ability of ICESat-2 ocean data to recover oceanographic signals ranging from surface gravity waves to the marine geoid. We focus on a region in the tropical Pacific and study photon height data in both the wavenumber and space domain. Results show that an ICESat-2 single track can recover the marine geoid at wavelengths > 20 km which is similar to the best radar altimeter data. The wavelength and propagation direction of surface gravity waves are sometimes well resolved by using a combination of the strong and weak beams, which are separated by 90 m. We find higher than expected power in the 3 km to 20 km wavelength band where geoid and ocean signals

should be small. This artificial power is caused by the projection of 2-D surface waves with ~300 m wavelengths into longer wavelengths (5-10 km) because of the 1-D sampling along the narrow ICESat-2 profile. Thus ICESat-2 will not provide major improvements to the geoid recovery in most of the ocean.

Key words: Satellite geodesy, Pacific Ocean, Wave propagation, Gravity anomalies and Earth structures

Subject: Gravity, geodesy and tides

1. Introduction

Over the past four decades, radar altimetry has been providing high-accuracy global sea surface height (SSH) measurements associated with the time-invariant marine geoid as well as dynamic oceanic variabilities. Several recent studies have highlighted the need to achieve 1 mGal gravity accuracy at a half wavelength spatial resolution of about twice the mean ocean depth (~ 8 km) to map small-scale tectonics, seamounts, and continental margin structure (e.g., Anderson et al. 2017; Sandwell et al. 2014). This 1 mGal objective corresponds to a sea surface slope accuracy of ~1 microradian or 8 mm over a distance of 8 km. The distance of 8 km corresponds to the optimal recoverable resolution of gravity anomaly from seafloor roughness, limited by the ocean depth due to upward continuation. The current best static gravity model based on all available repeat and non-repeat radar altimetry has reached an accuracy of 1 or 2 mGal in most ocean areas at a full-wavelength spatial resolution of 16-20 km (Sandwell et al. 2019).

At these small spatial scales, the largest error source in radar altimetry of sea surface

height is related to ocean surface gravity waves. The sharp outgoing radar pulse is blurred by

reflections from the peaks and troughs of the surface waves within the pulse-limited footprint of

the radar altimeter (3 km at 2 m significant wave height, SWH). Individual radar waveforms at a

20 Hz sampling rate have a range error of ~40 mm (Zhang et al. 2017). Better range precision of

about 20 mm has been achieved by SARAL/ALtiKa which operates at a shorter wavelength and

has a higher bandwidth and pulse repetition frequency. Further gravity improvements with pulse-

limited radar altimetry will be gradual as the noise is reduced as the square root of the number of

observations. Here we investigate the laser altimeter data from the Ice, Cloud, and land Elevation

Satellite 2 (ICESat-2) to better understand its potential contributions to gravity field recovery as

well as to understand how surface waves and other oceanographic signals degrade radar range

precision.

ICESat-2, which launched in September 2018, uses lidar to measure elevation with a

primary focus on the cryosphere and a tertiary objective of ocean topography. The Advanced

Topographic Laser Altimeter System (ATLAS) onboard splits the green laser into six beams

arranged in three pairs. Each pair consists of a strong and a weak beam with an energy ratio

about 4:1. The beams are separated by 90 m in the cross-track direction and by ~2.5 km in the

along-track direction. The three beam pairs are 3.3 km apart in the cross-track direction (Smith et

al. 2020). The round-trip travel times of photon beams that reflect from the ocean surface

provide estimates of height above a reference ellipsoid with 10 m horizontal accuracy and 0.03 m

vertical precision (Smith et al. 2020). ICESat-2 has a high sampling rate (10 kHz), narrow

footprint (15 m in diameter), near-global coverage (92° inclination), and a 91-day repeat. Around 10^{14} photons leave the ATLAS sensor per laser shot. Among photons that are reflected off the ocean surface, only 0-4 per laser shot travel back to the ATLAS because the open ocean has low reflectance in the visible spectrum (Hartmann 1994; Neumann et al., 2020). The ocean signal rates are similar to land. Neuenschwander & Magruder (2016) initially showed that ICESat-2 is able to accurately retrieve terrain heights from photon signal aggregation, which can be applied to surface wave characterization. Over the ocean, ICESat-2 is proven to allow for imaging individual waves (Klotz et al. 2019), and the signal that it detects is influenced by a mixture of surface and internal waves, tides, and balanced flows.

Each ICESat-2 ATLAS data set begins with the prefix "ATL". All products and related documents can be accessed through the National Snow & Ice Data Center. The ICESat-2 team provides a standard ocean height product ATL12 (Morison et al. 2020) which takes in ATL03 photon heights (Neumann et al., 2020) and outputs heights at a variable spacing (5-7 km over the tropical Pacific) along with SWH and statistics. Although ATL12 aims to achieve 10 mm accuracy for mean sea surface (MSS) height (Morison et al. 2020), the 5-7 km along-track sampling of that product is not adequate for our analysis which investigates the adverse effects of surface gravity waves on the recovery of the MSS.

The fine spatial resolution of ICESat-2 photon height data (~15m) motivates us to investigate its potential for ocean topography recovery. In this paper, we divide the ocean topography signals into three wavelength bands: MSS (MSS = geoid + mean dynamic

topography, >20 km); surface gravity wave band (<3 km); and the less well understood

intermediate band (3-20 km). We address the following questions: (1) Can the ICESat-2 ocean

data be used to improve the accuracy and resolution of the marine geoid and gravity field? (2)

What type of filter is best for the recovery and removal of sea surface signals that have scales

less than 3 km in wavelength? (3) What is the origin of the height signal in the intermediate

band range (3-20 km)? We address these questions by investigating ICESat-2's photon height

profiles in an area of the tropical Pacific (longitude -120° to -100°, latitude -11° to -1°) having

relatively low mesoscale ocean variability (Tchilibou et al. 2018) and calm sea state, with typical

SWH less than 2 m (Stopa 2019). These height profiles measure the MSS as well as temporal

variations associated with tides, ocean currents, and gravity waves.

The ICESat-2 ATL03 photon height data are analyzed in both the wavenumber domain

and the space domain. The wavenumber domain analysis reveals the full spectrum of height

variations over wavelengths from 50 m to 500 km. In addition, cross-spectral analysis among the

three strong lidar beams, as well as a MSS height model (MSSCNESCLS19), which is based on

all available radar altimeter data (Schaeffer et al. 2018) with 16-20 km spatial resolution, reveals

the best spatial resolution that is consistently recorded in ICESat-2 tracks. This wavenumber

analysis also provides the rationale for the design of along-track filters to separate the signal and

noise components. We then use band-pass filters to analyze the signal and noise of the ICESat-2

data in the space domain. We also generate synthetic sea surface height fields using wave buoy

data to assist understanding the 1-D sampling of 2-D surface waves. In addition, we show that

there are errors related to ocean surface gravity waves contaminating ICESat-2 observations in

two ways: (1) surface waves are energetic and need to be reduced by averaging repeating

observations; (2) surface waves in the 1-D sampling of laser altimeters could be projected to much longer apparent wavelengths and contaminate longer wavelength signals (5-10 km and longer).

2. Wavenumber Domain Analysis

We choose ATL03 geolocated photon heights in a 20° by 10° tropical Pacific box (longitude: -120° to -100°, latitude: -11° to -1°), selected because of its low variability in dynamic ocean topography. We use the strong beam photon heights that have medium and high confidence values. We assembled all strong beam profiles having more than 70% cloud-free data spanning the time period from December 2018 to May 2020. About 15% of the profiles satisfy these criteria (341 out of 2325 profiles). Heights were corrected for solid earth tides, solid earth pole tides, ocean loading and ocean pole tides, and referenced to the WGS84 ellipsoid (Neumann et al., 2020). We further apply ocean tides and inverse barometer corrections to the geolocated photons using geophysical corrections provided in the ATL03 dataset. Original data are sampled at 10 kHz, which corresponds to roughly 0.7 m in the along-track direction. We re-sample the data at 5 m intervals using a robust median, low-pass Gaussian filter with 0.5 gain at 30 m wavelength with the robust option in the Generic Mapping Tools "filter1d" function (Wessel et al., 2013). Median filtering reduces potential contamination from large height outliers caused by scattering of photons in the atmosphere as well as reflections from the subsurface. The filtered heights are used for all the analysis that follows.

First, we calculate the power spectral density (PSD) of each height profile using the Lomb-Scargle method (Lomb 1976; Scargle 1982). Interpolating gaps in height profiles is not desirable considering the large percentage of missing data. The Lomb-Scargle method is a spectral analysis algorithm for irregularly sampled and gappy data that is widely used in the astronomy community. We finally average the 341 power spectra to obtain the PSD in the Pacific box, which is shown in Figure 1. The 99% confidence interval is shaded in red.
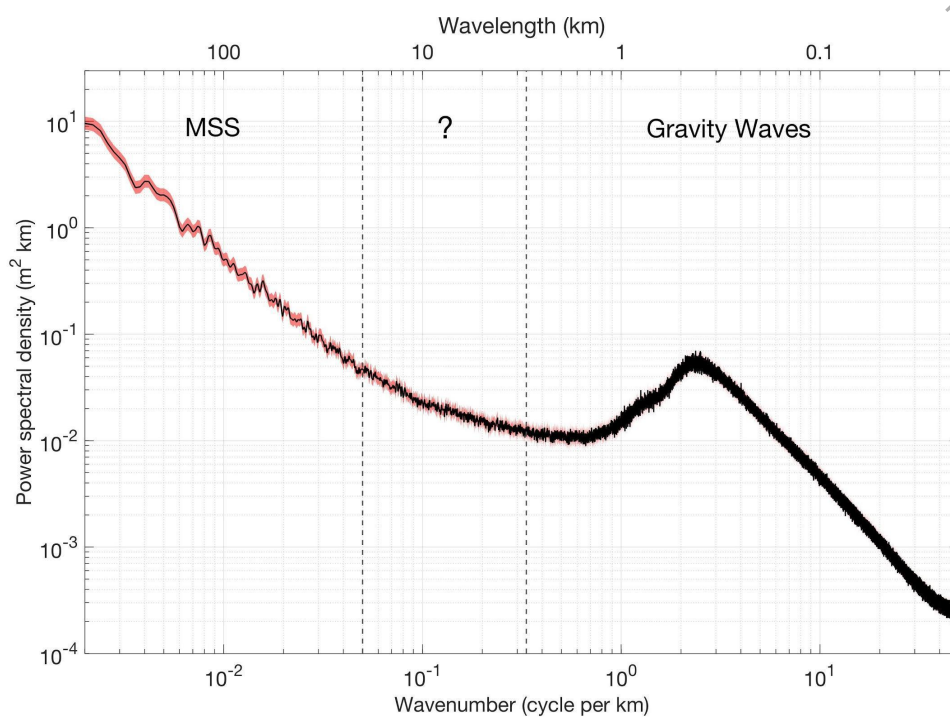

Figure 1. Averaged SSH power spectral density in the Pacific box. The spectrum can be divided into three bands representing long wavelength MSS signals (20-500 km), surface gravity waves (< 3 km), and the more poorly understood intermediate wavelength band (3-20 km). The 99% confidence interval is shaded in red.

From the average spectra (Figure 1), we identify three main spectral bands:

(1) The long-wavelength band (> 20 km) mainly reflects the MSS height which is a combination of time-invariant geoid height and mean ocean dynamic topography. We also use the MSSCNESCLS19 MSS model as the reference to remove the MSS and isolate the power spectrum of the sea level anomaly (SLA, Figure S1). Since the barotropic tides have also been removed, and there is no strong current in this tropical Pacific box, the remaining sea level variations are hypothesized to be primarily attributable to unbalanced flows and internal tides. This hypothesis is supported by the k^{-1} to k^{-2} spectral slope of SLA (Figure S1).

(2) The short wavelength part of the spectrum has a broad peak centered around 300 m. We show that this is mainly due to surface gravity waves. Note that the 341 profiles were collected at different times and thus sample different sea states, composed of waves with multiple wavelengths and directions. In particular, there is a wide range of possible wave directions α with respect to the ascending and descending tracks of the ICESat-2 orbit. This causes an increase in the apparent wavelength of the waves due to a $1/cos\,\alpha$ trigonometric relation.

(3) The power in the intermediate part of the spectrum is less well understood since this band is poorly sampled by radar altimeters because of their large pulse-limited footprint (3-5 km, Xu & Fu 2012). *In situ* measurements, i.e., ocean buoys, profilers, suggest two dominant types of ocean phenomena in this band: (i) Infragravity waves with wavelengths > 1 km typically have amplitudes of < 10 mm in the tropical Pacific (Aucan & Ardhuin 2013); (ii) High mode

internal waves/tides are also common and have amplitudes ~10 mm (Savage et al. 2017). Our

more detailed, space-domain analysis of the ICESat-2 data, provided below, shows

amplitudes of 100-200 mm in this band which is much larger than expected. A major focus

of this paper is to understand the source of these large amplitude signals. If they are true

oceanographic signals, they will be observed by the Surface Water and Ocean Topography

mission (SWOT) due to SWOT's high spatial resolution and 50-fold decrease in noise level

$(2 \text{ cm}^2/(\text{cycle/km}))$ (Desai et al. 2018). As we show further in this manuscript, it is more

likely that these large amplitude signals in intermediate wavelengths are due to instrument or

sampling issues.

To better understand the signal and noise characteristics of ICESat-2 as a function of

wavelength we perform two types of cross-spectral analyses. The first inter-compares the three

strong beams of individual tracks to understand the MSS resolution capability of ICESat-2. This

type of cross-spectral analysis is commonly used by the marine geophysics community to

characterize the shortest wavelength resolvable in the along-track altimeter data (Marks & Sailor

1986; Marks & Smith 2006; Yale et al. 1995). We select one profile (reference ground track:

0394, cycle: 02, segment number: 08, sensing time: 2019/01/23) in the Pacific Ocean with

latitudes ranging from -21.5° to -11° and compute cross-spectra for the height in the three

parallel strong beams. We use data with latitudes shifted to -21.5° to -11° that is beyond the

Pacific box because there is no gap larger than 10 km and fewer than 20% of data are missing for

all 3 beams. We interpolate gaps, detrend, apply a Von Hann taper (also known as the Hanning

window) to each 82 km segment, and use Welch's method to obtain the cross-spectrum

(including the coherence magnitude squared, or CMS, and phase), which is shown in Figure 2a and 2c.

In this inter-comparison, CMS is large at longer wavelengths where the MSS signal dominates, and it falls below the 95% confidence level (CL) at around 25 km (Figure 2a). The phase lag is around zero for the coherent wavelengths (Figure 2c). There are many factors that control resolution, including: gravity signal, oceanographic and instrument noise, ocean depth, and number of cycles (Yale et al. 1995). Here we analyze only one track consisting of three beams, which are separated by 3.3 km in the cross-track direction and have slightly different MSS. Low CMS does not necessarily mean that measurement noise dominates. Below, in the space domain analysis, we will show an example of high CMS at ~300 m wavelengths for strong and weak beams separated by 90 m in the cross-track direction; this high CMS is due to surface waves. Yet neighboring strong beams separated by 3.3 km are generally not coherent in the surface wave band.

The second coherence analysis uses the MSSCNESCLS19 MSS model as the reference for each of the strong beams. This MSS model has spatial resolution of 16 km so we cannot expect the analysis to reveal shorter wavelength signals in the altimetry but we can evaluate the accuracy at longer wavelengths (~20 km) and also indirectly compare the resolution of ICESat-2 with other altimeter data. We correct for cross-track MSS differences by removing the MSS at the location of each of the three beams and adding back the MSS for the center beam 2l. The spectral CMS and phase between each beam and the MSS are shown in Figure 2b and 2d. In this

case, the signal is the time invariant MSS, which is common to all three beams, and noise arises

from oceanic processes and measurement noise. This analysis shows statistically significant

CMS and low phase for wavelengths longer than 20 km. The greater CMS between the ICESat-2

profiles and the MSS compared to the inter-beam CMS is consistent with what we would expect

if we assume that ICESat-2 SSH beams contain noise while the MSS is noise free (Bendat &

Piersol 2011). A higher CMS limit could be achieved with multi-track stacking.
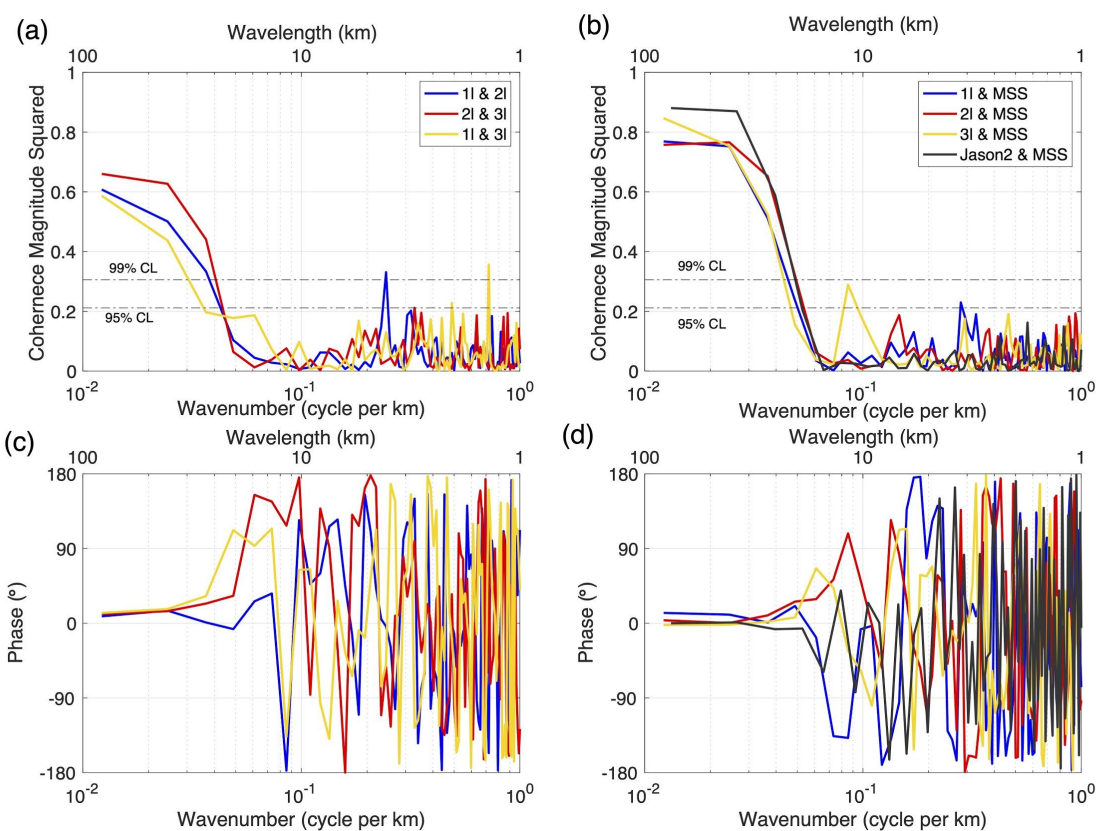
Figure 2. (a) CMS and (c) phase between beams 1l-2l, 2l-3l, 1l-3l of a selected ICESat-2 track

(ground track: 0394, cycle: 02). CMS falls to below 95% CL at ~25 km. (b) CMS and (d) phase

between MSS and each strong beam. Black line is the spectral CMS and phase between 20Hz Jason-2 and MSS. CMS falls to below 95% CL at ~20 km for both the ICESat-2 and the Jason-2 cases.

To compare these ICESat-2 results with radar altimetry, we analyzed 20 Hz sampled Jason-2 radar altimetry height profiles (cycle 233) and calculated their cross-spectrum with the MSS. The along-track spacing of Jason-2 is 296 m. We apply a 256-point non-overlapping Von Hann window (segment length is about 76 km) and use Welch's method to compute the spectral CMS and phase between Jason-2 and MSS, which is shown in Figure 2b and 2c in black lines. A shorter track is used in order to obtain the same number of segments as ICESat-2. We find that Jason-2/MSS drops to 99% and 95% CLs at similar wavelengths as the ICESat-2/MSS CMS. This suggests that ICESat-2 has signal and noise characteristics similar to those of Jason-2 in terms of MSS reconstruction, with a characteristic coherent length scale of about 20 km for a single pass. Although the analysis focuses on single ICESat-2 and Jason2 tracks, we have analyzed more tracks in the Pacific box and see that the results shown in Figure 2 are representative, when all three beams show good quality and have no major data gaps larger than 10 km.

3. Space Domain Analysis

Given these wavenumber domain analyses, we examine the signal and noise of ICESat-2 data in each of the three bands in the space domain using the same three strong beams (reference ground track: 0394, cycle: 02, segment number: 08, sensing time: 2019/01/23) as in Figure 2.

3.1. Long Wavelength Mean Sea Surface

The coherence analyses (Figure 2) suggest that the three beams all measure the same MSS at wavelengths greater than 20 km. A space domain example is shown in Figure 3 where each of the three beams was low-pass filtered using a Gaussian with 0.5 gain at 20 km. As described above, beams 1l and 3l were corrected to the location of the beam 2l, and a trend was removed from each. There is general agreement between ICESat-2 and radar altimeter derived MSS at long wavelengths. A shorter segment of the plotted beams (Figure 3b) reveals that the differences have amplitudes of ~0.03 m.
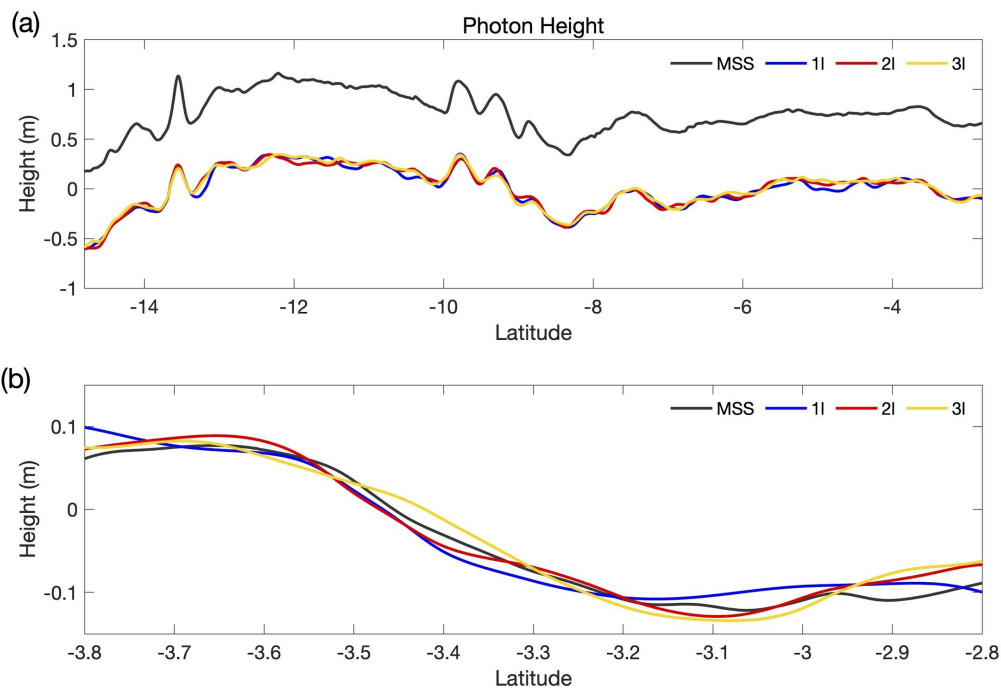

Figure 3. (a) SSH of ICESat-2 3 strong beams (ground track: 0394, cycle: 02) along with MSS at beam 2l's position. Data are low-pass filtered at 20 km, and the linear trend of beam 2l has

been removed from all four height series. The MSS is offset for plotting. (b) a shorter segment with no MSS offset. Tracks run almost north-south so 1° in latitude corresponds to ~110 km along track.

3.2. Short Wavelength: Surface Gravity Waves

To isolate the signals from surface waves, we first remove the MSS from each strong beam profile to create SLA (Figure 4). These profiles contain oceanographic signals and noise over the entire spectrum. Most of the cross-beam differences and along-track variations have a wavelength of a few hundred meters and are consistent with height signals from surface gravity waves (Figure 4b).
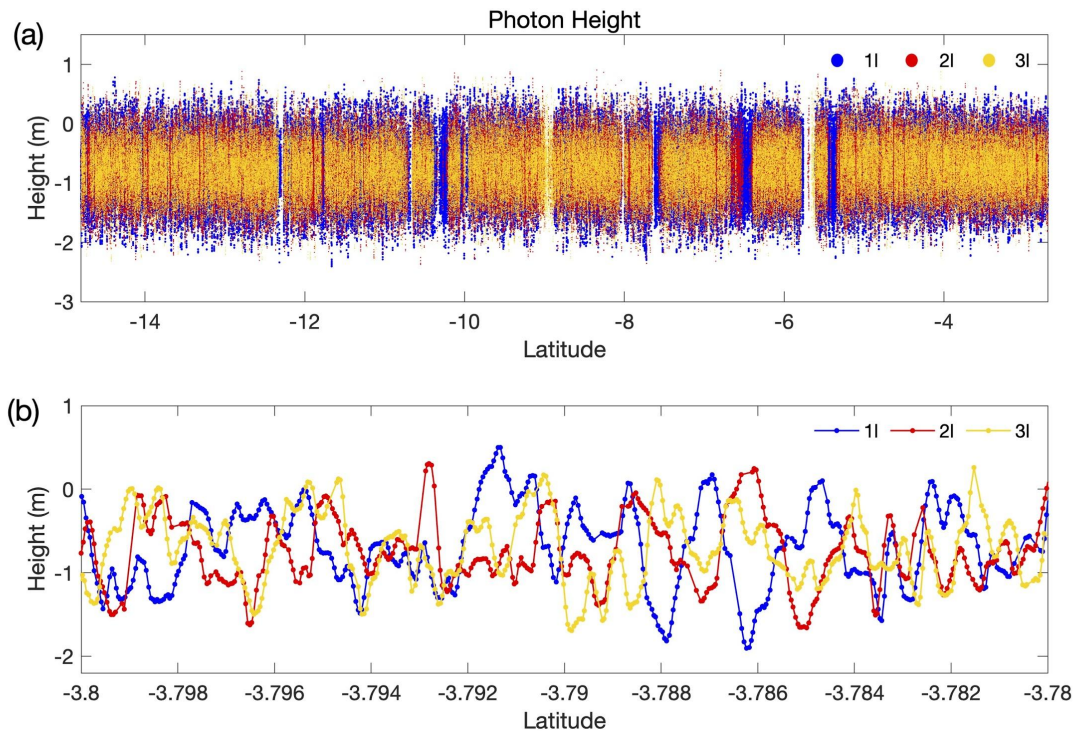
Figure 4. (a) SLA of ICESat-2 3 strong beams (ground track: 0394, cycle: 02). (b) a shorter

segment of (a) showing peak to trough variations having wavelengths of a few hundreds of

meters. Tracks run almost N-S so 1° corresponds to ~110 km along track and each 0.002° grid in

(b) is about 200 m.

3.2.1 Significant Wave Height Analysis

We further calculate the SWH from ICESat-2 SLA data. For radar altimetry, the SWH is

4 times the root-mean squared (rms) height variation in the 3-km pulse-limited footprint

averaging area, and it is derived from the rise time of the fit to the return waveform. To calculate

SWH for the ICESat-2 data, we first low-pass filter the SLA using a running mean over a 3 km

window. This is done to simulate the 3-km pulse-limited footprint of a radar altimeter. The rms difference from the mean, times 4, is further low-pass filtered over 6 km to simulate the 1Hz averaged SWH in radar altimetry. The results are shown in Figure 5 where the SWH varies between 1.5 m and 2 m, which is typical for this region (Stopa 2019; Dodet et al. 2020). Differences in SWH between the 3 beams can be up to ~0.3 m. This is to be expected since there could be sea state gradients over scales of kilometers.
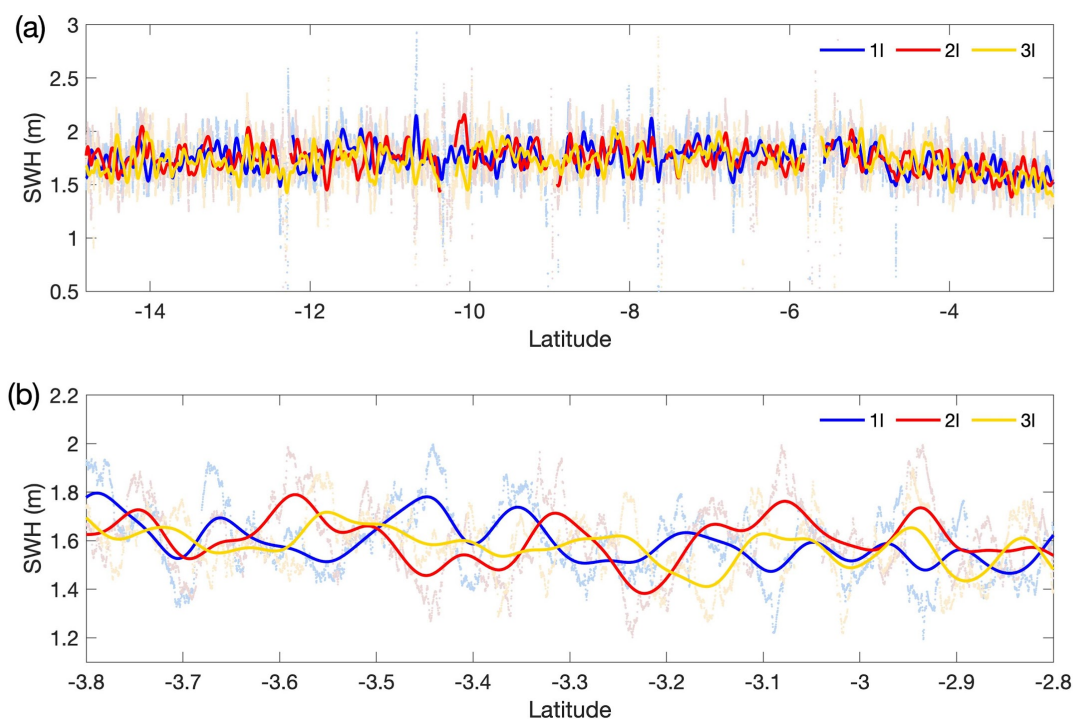

Figure 5. (a) SWH calculated from 3-km-running standard deviation of SLA from ICESat-2 3 strong beams (ground track: 0394, cycle: 02). Background light dots are SWH before filtering and darker lines are low-pass filtered at 6 km so that they resemble the 1Hz averaged SWH in

radar altimetry. (b) a shorter segment of (a). Tracks run almost N-S so 1° corresponds to ~110 km along track.

3.2.2. Dominant Ocean Wave Reconstruction

We can further analyze the surface gravity wave signal using the strong/weak beam pairs spaced at 90 m. Considering that weak beam data have very limited photon recovery from the ocean surface, the analysis here is applied to segments with a minimum length of 20 km, where a pair of strong and weak beams both have collected good-quality photon data. Each pair of strong and weak beams is generally highly coherent since the 90 m cross-track distance is less than the average wavelength of surface waves (including swell and wind seas) in this region (Young 1999; Arinaga & Cheung 2012). The wavenumber of the CMS peak identifies the wavelength of the dominant wave projected in the orbit direction. The spectral phase is the relative phase shift between two beams, and we can use it to reconstruct wave direction, though with a 180° ambiguity. We can further recover the true wavelength by combining wave direction and projected wavelength (details are provided in supporting information). There is also ~2.5 km along-track offset between each pair of strong and weak beams, as the weak and strong beam pairs are offset relative to each other. This corresponds to ~0.35 s shift in time during which surface waves only travel a few meters. We identify phase shift from this time delay to error in wave reconstruction. This error has little influence on the CMS but will shift the phase by up to 10°. Figure 6 shows an example where a weak beam leads a strong beam in an ascending track. Statistically significant CMS over wavelengths in the swell band (100-1000 m) peaks around 465

m (observed wavelength in the orbit direction) with a phase shift of -70.3°. These two effects are consistent with a 327±16.8 m swell wavelength coming from an azimuth of 223.3±7.3° (clockwise from north). The error ranges are obtained via the following steps: (i) dividing the beam pair into 11 equal-length segments, each subdivided into 10 short segments that are used to calculate the coherence between the strong and weak beams; (ii) bootstrapping the 11 sets of coherence results over 100 realizations and calculating the 95% confidence interval. This reconstruction from ICESat-2 observations agrees with a WAVEWATCH III hindcast multigrid product (Chawla et. 2012), which uses the operational National Centers for Environmental Prediction winds and ice fields as input forcing fields and is independent of altimetry observations. WAVEWATCH III provides a predicted wavelength of 336.0±15.9 m and azimuth of 209.8±1.6° at the nearest grid point and the closest time. The error ranges for WAVEWATCH III hindcast wavelength and direction come from the 95% confidence interval of data collected in a 7°×7° region over 9 hours.
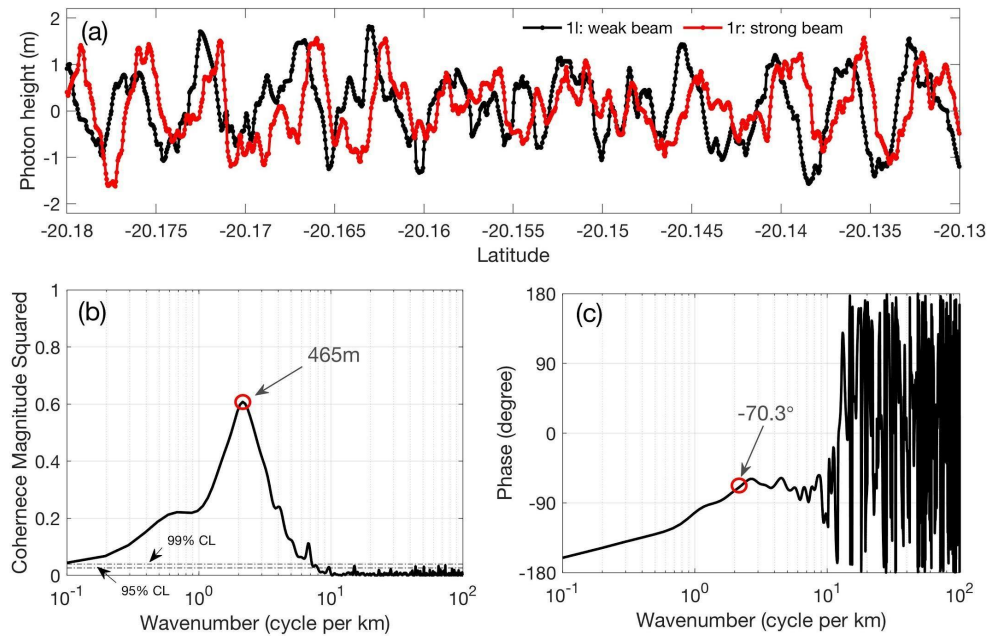
Figure 6. (a) a small segment of ICESat-2 photon height data w.r.t WGS 84. (ground track: 0326, cycle: 01). The strong and weak beams are separated by 90 m and both are low-pass filtered at 30 m. (b) CMS and (c) phase between beams 1l and 1r. Coherence peaks around 465 m, and the corresponding phase shift is -70.3°. The 99% and 95% CL are labeled.

We have performed 456 sets of strong/weak beam analysis in the tropical Pacific region to establish the wavelength and wave direction from ICESat-2 photon data and compare the results with predictions of peak direction and peak wavelength from the WAVEWATCH III model at the grid point closest to the middle of each track. We also calculated the SWH from each set of beam pairs and made a comparison with the WAVEWATCH III model. The results are provided in Figure 7. Figure 7a-c shows joint probability histograms for wavelength, wave directions and SWH of WAVEWATCH III predictions and ICESat-2 pairs. In the histograms,

wavelengths are binned by 50 m increments and directions by 15 degree increments. The SWHs are rounded to the nearest multiple of 0.2 m. Histograms of ICESat-2 and WAVEWATCH III differences are shown in Figure 7d-f, respectively. The ICESat-2 reconstructed wavelengths are slightly longer, and the best fit ICESat-2 to WAVEWATCH III wavelength slope is 1.11 with intercept set to zero. The histogram of wavelength differences (Figure 7d) has a quasi-Gaussian shape and is slightly biased to the positive with a mean difference μ of 57.3 m, and root mean square error (RMSE) of 151.0 m. The ICESat-2 reconstructed wave directions are generally between 0°-60° and 120°-180°, as waves propagating orthogonally to satellite ground tracks are less likely to show coherence between a pair of strong and weak beams. A regression of ICESat-2 to WAVEWATCH III directions shows that for the propagation directions from 0°-60°, ICESat-2 propagation directions are about 81% of WAVEWATCH III directions. The histogram of wave directional differences (Figure 7d) centers around zero, although it spreads widely from -90° to 90° (directional differences larger than ±90° are indistinguishable from directional differences between -90° and 90°; the plot shows only the smallest possible directional difference). The mean value of direction differences μ is 20.5°, and the RMSE is 69.4°. For SWH, the ICESat-2 values compare well with WAVEWATCH III, with a mean difference of -0.04 m and RMSE of 0.34 m, which is similar to the result in Klotz et al. (2019), who compared ICESat-2 and the ERA-5 reanalysis in the Atlantic Ocean. The ICESat-2 SWHs are slightly small and are about 0.96 of WAVEWATCH III SWH.
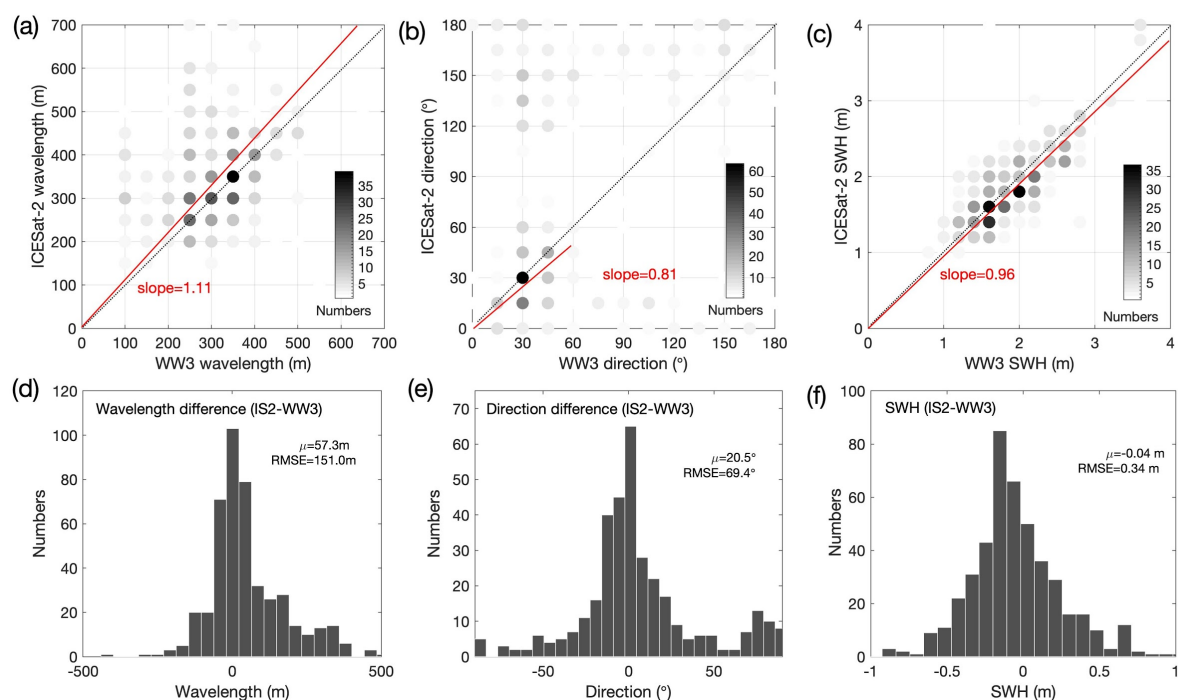
Figure 7. Joint probability histograms for (a) wavelength, (b) wave directions and (c) SWH of WAVEWATCH III (WW3) predictions and ICESat-2 (IS2) reconstructions. The black dotted line is the 1:1 relationship and the red line is the best fitted slope. Histogram of (d) wavelength, (e) direction and (f) SWH differences between IS2 reconstructions and WW3 predictions. The mean μ and RMSE of wavelength/direction/SWH differences are shown in (d)-(f).

3.3. Sea Level Anomalies at Wavelengths > 3 km

Finally, we investigate the SLA for wavelengths > 3 km. We low-pass filter ICESat-2 SLA using a Gaussian with a 0.5 gain at 3 km to remove most of the signals from the surface gravity waves and isolate other oceanography signals (see Figure 8). The low-pass filtered SLA

shows much smaller amplitude (0.1-0.2 m) than the full band SLA in Figure 4 (~1 m). All three

beams show a common undulation having a characteristic wavelength of about 400-500 km. This

signal is likely due to the dynamic topography of the ocean caused by currents or tide-model

error, as it also shows up in other cycles of the same ground track, but in different phases.

In addition to this expected longer wavelength oceanographic signal, there are rather

large signals (0.1-0.2 m) with wavelengths of 5-10 km (Figure 8b). As noted in the introduction

we expected that oceanographic signals should be 10 times smaller in this wavelength band

(Savage et al. 2017; Aucan & Ardhuin 2013). Moreover, if they are due to ocean phenomena

with length scales of 5-10 km, then the signals should be coherent among the three beams.

However, in our coherence analysis (Figure 2), we show that the three beams are incoherent over

this band. The remaining explanations for these signals are either that errors in the ICESat-2

photon data are different among the three beams or that shorter wavelength signals are projected

into longer wavelengths. We note that the ICESat-2 sampling is a very narrow 1-D track sample
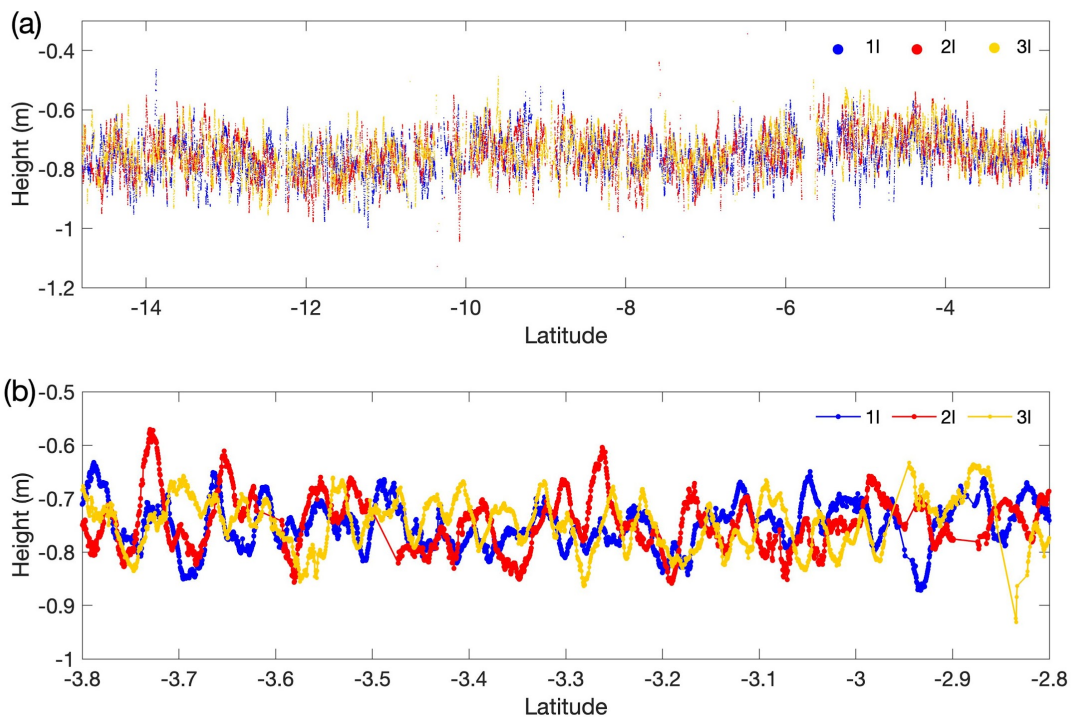
of a 2-D ocean surface.

Figure 8. (a) Low-pass filtered (3 km and sampled at 50 m) SLA. Missing data were not included in the filter. (b) a shorter segment of (a). Tracks run almost N-S so 1° corresponds to ~110 km along track.

3.3.1. 1-D Sampling of a 2-D Ocean Waves

The largest signal in the ICESat-2 SLA data is due to surface waves. If the dominant wave direction is roughly aligned with the direction of an ICESat-2 track, then the 3 km low-pass filter will remove this signal, leaving behind an essentially flat SLA. However, if the wave direction is nearly perpendicular to the track, the ocean swell having characteristic wavelengths

of a few hundred meters will be projected to wavelengths longer than 3 km. Next we illustrate

the extent of this projection.

Assume there is a plane wave with wavelength L_0 and amplitude A coming from the

north ($\theta = 0°$), then the SSH (η) due to the wave can be described as:

$$\eta(x, y, t) = A cos(ky - \omega t + \varphi),$$

<div align="right">(1)</div>

where x is in the eastward direction and y is northward, $k = \frac{2\pi}{L_0}$ is the horizontal wavenumber,

$\omega = \sqrt{gk}$ is the angular frequency ($g = 9.81$ m/s^2 is the gravitational acceleration), and φ is

the initial phase. In the 1-D sampling of a satellite flying from direction θ_0 (north: 0°, east: 90°)

at a ground speed of V_s (~7 km/s), the observed along track wave height should be:

$$\eta(S, t) = A cos\left(k\ S cos\ \alpha - \omega\frac{S}{V_s} + \varphi\right) = A cos\left(\left(k\ cos\ \alpha - \frac{\omega}{V_s}\right)S + \varphi\right),$$

<div align="right">(2)</div>

where $\alpha = \theta - \theta_0$ is the angle between wave direction and orbit, $S = y/\cos \alpha$ is the along-track distance. The observed wavenumber k' is:

$$k' = k \left(\cos \alpha - \frac{\omega}{V_s} \right),$$

(3)

and the observed wavelength L' is:

$$L' = \frac{2\pi}{k \left(\cos \alpha - \frac{\omega}{V_s} \right)} = L_0/(\cos \alpha - \frac{\omega L_0}{2\pi V_s}) \approx L_0/\cos \alpha.$$

(4)

ICESat-2 has a ground velocity of 7 km/s so waves propagating at an angle α with respect to the track will shown an apparent wavelength that is longer by around $1/\cos \alpha$. As $\cos \alpha$ approaches zero, the satellite ground speed becomes increasingly important. For example, for a 200 m plane wave, when $\alpha = 88°$, the satellite will observe an 8 km apparent wavelength; when $\alpha = 90°$, the apparent wavelength is 79 km. This projection pattern is a particular challenge for ICESat-2's small footprint, as it implies that any component of 50-300 m surface wave crests

aligned with the satellite orbit could project to wavelengths of 20 km or longer. Because surface gravity waves are energetic compared with the background large-scale sea surface height, even low-amplitude waves have the potential to fill in the intermediate portion of the spectrum.

In the extreme case of the waves propagating in a direction nearly perpendicular to the track with the relation $cos\ \alpha\ = \frac{\omega L_0}{2\pi V_s}$ (α=89.855° if L_0=200 m; α=89.771° if L_0=500 m), ICESat-2 will only sample a single height, so the observed wavelength will be shifted away from the true wavelength to infinitely long scales, and all three beams will be measured as different heights depending on the phase of the waves they sample. Here we assumed only a plane wave case which does not capture the complexity of true sea states, so we need to investigate how ICESat-2 would sample a more realistic ocean surface.

3.3.2. Synthetic Wave Field Analysis

To generate a realistic 2-D sea state we use a time series of ocean surface elevation collected from a 3-component GPS receiver on a wave buoy. There are no wave buoys in our South Pacific box so we selected buoy data from the Coastal Data Information Program (CDIP) at station Point Reyes, off the California coast (latitude: 37.94 °N, longitude: -123.46 °E, depth: 550 m, time: 2019-09-29, 19:00 UTC). This buoy is located in deep water, so we will assume that waves follow the deep water dispersion relation. Although the CDIP directional spectrum only reflects the wave conditions at a specific point, time-averaged over half an hour, it

provides realistic statistics of waves coming from all directions to generate a surface wave-only SSH field.

We generate finite length, 2-D synthetic sea surface elevations by assuming that the sea state results from the linear superposition of all wave components measured by the wave buoy and assigning random phases to the amplitudes. To avoid the extreme case of waves being projected to infinitely long scales in the ICESat-2 orbit direction (182°), we omit a 2 degree range of the 2-D wave spectrum (91°-93°, 271°-273°, white area in Figure 9a). The directional wave spectrum as a function of wave period and direction (Figure 9a) was computed from the angular moments provided by CDIP using the maximum entropy method (Lygre & Krogstad 1986). The wave period varies between 1.72 s and 40 s, with a corresponding wavelength between 5 and 2500 m. In this case study, most energy comes from 330° (northwest), and there is almost no energy for waves longer than 20 seconds (~624 m in wavelength). In addition to the most energetic wave systems, coming predominantly from 330°, the wave field at this specific time and location also contains some wave energy at periods between 8 s and 13 s (100 m to 264 m in wavelengths) that is spread across directions between 240° and 360°. It is also worth noting that there is some energy in direction bins that are nearly perpendicular (e.g. from ~269°) to the ICESat-2 trackline. In this case, the 1-D sampling will increase the apparent wavelength of these waves by a factor of ~20, so the energy of a 300 m wave would appear as a 6 km wavelength signal. The questions now are: what is the amplitude of this effect, and can it explain the observations in the 3-20 km wavelength shown in Figure 8?
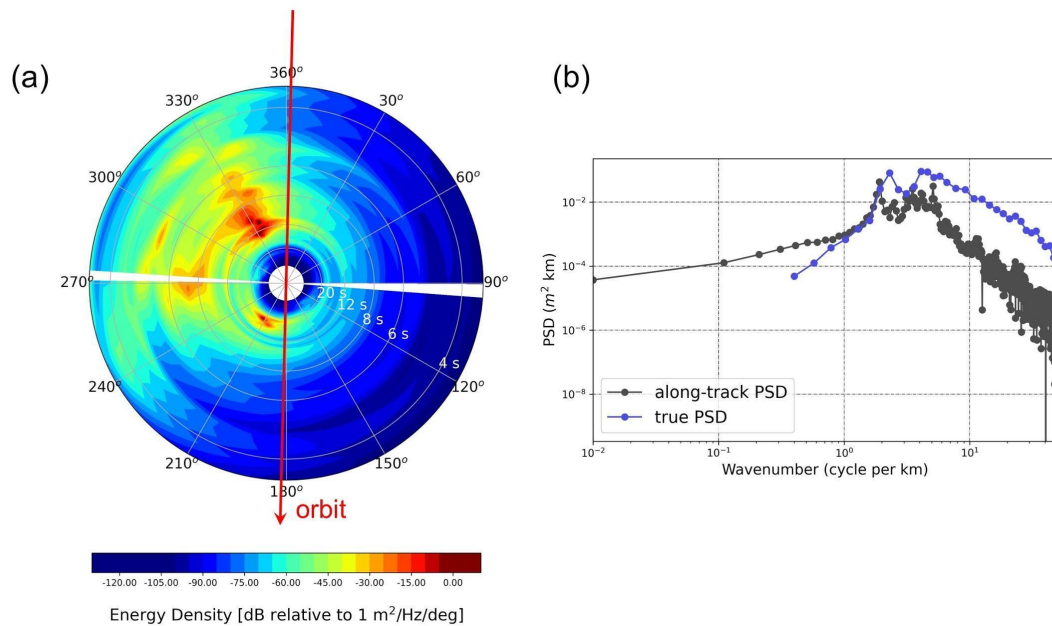
Figure 9. (a) Directional spectrum from CDIP station Point Reyes at time: 2019-09-29, 19:00 UTC. Energy density is in dB so as to show a large range of energy levels. The directional spectrum was computed using the maximum entropy method (Lygre et al. 1986). ICESat-2 orbit inclination is 92° and here we show a synthetic descending track (in red). (b) gray: along-track PSD; blue: true PSD. Both are derived from the directional spectrum in (a).

We use the CDIP directional spectrum and positions of the ICESat-2 beams (ground track: 0394, cycle: 02) to take one-dimensional (1-D) samples of the 2-D synthetic sea surface elevations in the ICESat-2 orbit direction. Following this method we generate three synthetic SLA profiles spaced by 3.3 km. We then apply a 3 km low-pass Gaussian filter. The synthetic profiles and 3 km low-pass filtered results are shown in Figure 10. We compute a 3 km running standard deviation of the synthetic SLA profiles and then multiply by 4 to get the SWH, which is around 1.95 m with 0.4 m variation in amplitude. The SWH of synthetic along track SLA is

smaller than the true SWH of 2.79 m from the CDIP buoy observations. While the synthetic SLA

signals are realizations of surface gravity waves with wavelength less than 1 km, there are 0.2 m

undulations with wavelengths of 5-10 km in the low-pass filtered SLA (Figure 10b), which result

from short wavelength surface waves projected to much longer wavelengths in 1-D sampling
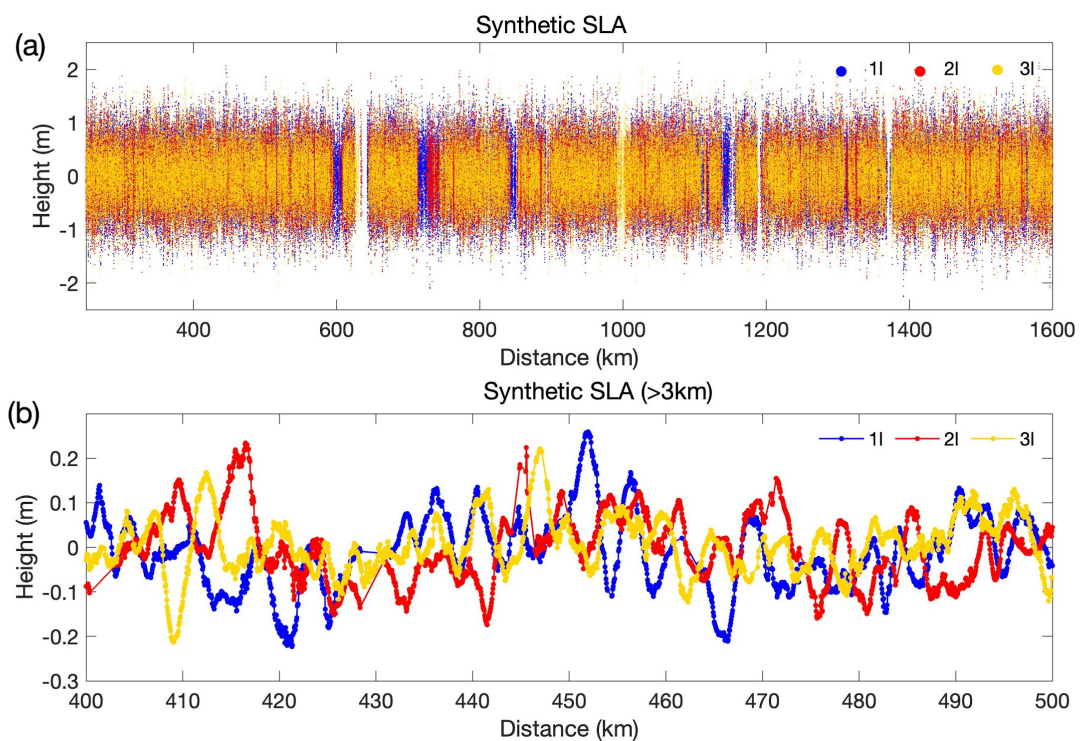
profiles.

Figure 10. (a) Synthetic SLA using CDIP directional spectrum in Figure 9a and the positions of

ICESat-2 track (ground track: 0394, cycle: 02). (b) 3 km low-pass filtered synthetic SLA for a

100-km segment.

To support our findings, we calculate the true PSD as well as the along-track PSD — as it would be observed by ICESat-2 — as a function of wavenumber (Figure 9b). The true wavenumber PSD $E(q)$ (Figure 9b, blue) is obtained from the CDIP frequency spectrum $E(f)$ using the deep water dispersion relation:

$$\omega^2 = \frac{2\pi g}{L} = 2\pi g q,$$

(5)

where $\omega = 2\pi f$ is the angular frequency, L is the wavelength, and $q = 1/L$ is the wavenumber, such that

$$E(q) = \frac{g}{4\pi f} E(f).$$

(6)

We calculate the along-track PSD (Figure 9b, gray) that would be observed by ICESat-2 following the steps below:

(i) Convert the observed directional wave spectrum $E(f, \theta)$ with dimensions of

m^2/Hz/degree in Figure 9a to a function of wavenumber and direction $E(q, \theta)$ with

dimensions of m^3/degree, following the deep water dispersion relation (5)

$$E(q, \theta) = \frac{g}{4\pi f} E(f, \theta).$$

(7)

(ii) Project the wavenumbers q from the wave direction θ to the orbit direction θ_0

$$q' = q \cos \alpha,$$

(8)

where q' is the wavenumber projected to the along-track direction, and $\alpha = \theta - \theta_0$ is the

angle between the wave direction and the orbit direction.

(iii) We then create equally spaced along-track wavenumber bins q_s ranging from

0.01cpkm to 250.01cpkm with a spacing of 0.1 cpkm, and, for each bin, the along-track

energy density $E(q_s)$ is the integral of the projected energy density $E(q, \theta) \cos \alpha$ over all

grid points where $q' = q_s$.

As an example of the steps above, let us consider waves coming from $\theta = 332°$ with a period of

12 s and wavenumber $q = 4.45$ cpkm ($L = 225$ m). In the 1-D sampling from ICESat-2's

descending orbit ($\theta_0 = 2°$), the satellite would observe an apparent wavenumber $q' = 3.86$ cpkm

($L' = 225$m/cos(330°) = 259 m). We would then integrate all projected wave energy associated

with an apparent wavenumber in the 3.81-3.91 cpkm bin to get the corresponding spectral energy

at that bin in the along-track PSD (Figure 9b, in gray).

We compare the along-track PSD and the true PSD in Figure 9b to guide our

interpretation of 1-D wave behavior. In general, in the along-track PSD, there is decreased

energy at the high wavenumber end (>5 cpkm) and extra energy associated with low

wavenumbers (<0.3 cpkm) that are beyond the surface gravity wave range. Short-wavelength

surface waves are projected to longer apparent wavelengths in the along-track direction; if they

propagate in a direction nearly perpendicular to the orbit direction, surface waves could be projected to much longer wavelengths (>3 km). There are several shifted swell peaks, including 1) the ~16s wave (430 m in wavelength, 2.3 cpkm in the true PSD) from direction 213° projected to 2 cpkm in the along-track direction; 2) the ~12.5s (244 m in wavelength, 4.1 cpkm in the true PSD) wave from direction 330° projected to 3.5 cpkm.

In the ocean, surface waves propagate from all directions with a broad range of frequencies and amplitudes of the order of 10 cm or more. If the wave field is fully isotropic, then an along-track spatial average of ICESat-2 measurements will minimize surface wave effects. As the example in Figure 9a indicates, often a single wavenumber and direction dominate the wave field. Problems will arise when the dominant surface wave crests align with the orbit direction, so that waves appear to have wavelengths of ~10 km or more. In these cases a low-pass filter will not be able to suppress effects due to surface waves.

4. Discussion and conclusions

We have studied the ability of ICESat-2 photon height data to recover oceanographic signals ranging from surface gravity waves to the marine geoid using data over a tropical Pacific box in both the wavenumber domain and space domain. We analyze the data in three bands: long wavelengths (20-500 km), intermediate wavelengths (3-20 km), and short wavelengths (15 m-3 km).

At long wavelengths, we use coherence to compare the three parallel beams of ICESat-2, as well as a high resolution MSS model based on radar altimetry, to show that the single track can recovery along-track MSS with wavelength about 20 km, which is similar to the best radar altimeters. However, ICESat-2 data are not as continuous as radar altimeter data. There are large gaps due to clouds and smaller gaps because the open ocean has low reflectance in the visible spectrum. Data gaps complicate the usage of ICESat-2 photon data on global scales.

At short wavelengths we find that ICESat-2 provides accurate and high-resolution profiles of surface waves in agreement with previous studies (Klotz et al. 2019). Moreover, data from a pair of strong and weak beams, separated by 90 m, can be used to estimate the dominant wave direction and wavelength. The wave reconstruction in this study (see Figure 6 and 7) is only tentative, yet it demonstrates ICESat-2's potential in monitoring global ocean wave conditions, especially in the south Pacific Ocean where in situ wave measurements are not usually available. Estimates of SWH from ICESat-2 data generally agree well with WAVEWATCH III hindcasts and independent buoy measurements (Klotz et al. 2020). As directional wave spectrum measurements from the Chinese-French Oceanography Satellite (CFOSAT) become available, the method proposed here could be further validated in the open-ocean without having to rely exclusively on wave model output.

We find that signals in the intermediate wavelength band from 3-20 km provided by ICESat-2 are 10-20 times more energetic than expected (Aucan & Ardhuin 2013; Savage et al. 2017). The sea state is generally determined by a superposition of long-period, narrow-banded

swell and short-period, locally generated wind seas, having a wide range of wavelengths and directions (Sverdrup & Munk 1947; Villas Bôas et al. 2017). ICESat-2 samples this 2-D wave field with a narrow beam in 1-D so the wavelength of surface waves observed by ICESat-2 is always greater than the true wavelength. For example, a 300 m swell having a 0.2 m amplitude and an orientation of 87° with respect to the ICESat-2 track will project into a signal with the same amplitude at 6 km wavelength. The three beams have a wide enough spacing to provide independent estimates of this projected swell, so averaging the three beams could reduce this projection by 1.7 times but not the 10-20 times needed for accurate measurements in this band. Note that pulse-limited radar altimeters do not suffer from this projection. A typical footprint diameter of a radar altimeter is 3 km at a 2 m SWH. Therefore there is a natural 2-D low-pass filter applied during the interaction of the radar pulse with the ocean surface waves. This suppresses all the wave energy shown in the spectra in Figure 9a. Nevertheless the wave noise re-appears as a smoothing of the radar return pulse that reduces the precision of measurement of the arrival time of the radar pulse.

To conclude, ICESat-2 is a highly capable instrument with the potential to yield new information about along-track surface waves over distances of 10 km or less, but it will not provide major improvements to the geoid in the open ocean, where many years of radar altimeter observations are providing increasingly accurate global marine gravity maps approaching 12 km wavelength resolution. However, ICESat-2 data may be valuable in regions where surface gravity waves have low amplitude, and the broad radar altimeter waveforms are corrupted by land reflections in a 5 km radius.

Data Available Statement

ICESat-2 data are provided by NASA and available through the National Snow & Ice Data Center (NSIDC). The geolocated photon data are downloaded from: https://nsidc.org/data/atl03. The MSSCNESCLS19 model is from Philippe Schaeffer and David Sandwell and is available upon request (dsandwell@ucsd.edu). The Jason2 20Hz sea surface height data are from: https://openadb.dgfi.tum.de/en/. The WAVEWATCH III global multigrid hindcast products are available through: https://polar.ncep.noaa.gov/waves/hindcasts/prod-multi_1.php.

Conflict of Interests

The authors declare no conflicts of interest relevant to this study.

References

Arinaga, R. A., & Cheung, K. F. (2012). Atlas of global wave energy from 10 years of reanalysis and hindcast data. *Renewable Energy*, *39*(1), 49-64.

Aucan, J., & Ardhuin, F. (2013). Infragravity waves in the deep ocean: An upward revision. *Geophysical Research Letters*, *40*(13), 3435-3439.

Andersen, O. B., Knudsen, P., Kenyon, S., Factor, J. K., & Holmes, S. (2017). Global gravity field from recent satellites (DTU15)—Arctic improvements. *First Break*, 35(12).

Bendat, J. S., & Piersol, A. G. (2011). *Random data: analysis and measurement procedures* (Vol. 729). John Wiley & Sons.

Callies, J., & Wu, W. (2019). Some expectations for submesoscale sea surface height variance spectra. *Journal of Physical Oceanography*, *49*(9), 2271-2289.

Chawla, A., Spindler, D., & Tolman, H. (2012). 30 Year Wave Hindcasts using WAVEWATCH III with CFSR winds Phase. *NOAA/NWS/NCEP/MMAB. Maryl. USA*, *23*.

Desai, S., Fu, L. L., Cherchali, S., & Vaze, P. (2018). Surface Water and Ocean Topography Mission (SWOT) Project science requirements document. In *Tech. Rep. JPL D-61923*. National Aeronautics and Space Administration, Jet Propulsion Laboratory. https://swot.jpl.nasa.gov/system/documents/files/2176_2176_D-61923_SRD_Rev_B_20181113.pdf

Dodet, G., Piolle, J. F., Quilfen, Y., Abdalla, S., Accensi, M., Ardhuin, F., ... & Passaro, M. (2020). The Sea State CCI dataset v1: towards a sea state climate data record based on satellite observations. *Earth System Science Data*, *12*(3), 1929-1951.

Klotz, B. W., Neuenschwander, A., & Magruder, L. A. (2019). High-Resolution Ocean Wave and Wind Characteristics Determined by the ICESat-2 Land Surface Algorithm. *Geophysical Research Letters*, *47*(1), e2019GL085907.

Lygre, A., & Krogstad, H. E. (1986). Maximum entropy estimation of the directional distribution in ocean wave spectra. *Journal of Physical Oceanography*, *16*(12), 2052-2060.

Marks, K. M., & Sailor, R. V. (1986). Comparison of Geos-3 and Seasat altimeter resolution capabilities. *Geophysical research letters*, *13*(7), 697-700.

Marks, K. M., & Smith, W. H. F. (2006). An evaluation of publicly available global bathymetry grids. *Marine Geophysical Researches*, *27*(1), 19-34. https://icesat-2.gsfc.nasa.gov/sites/default/files/page_files/ICESat2_ATL12_ATBD_r002.pdf

Morison, J. H., Hancock, D., Dickinson, S., Robbins, J., Roberts, L., Kwok, R., Palm, S. P., Smith, B., Jasinski, M. F. and the ICESat-2 Science Team. (2020). ATLAS/ICESat-2 L3A Ocean Surface Height, Version 3. Boulder, *Colorado USA. NASA National Snow and Ice Data Center Distributed Active Archive Center*, https://doi.org/10.5067/ATLAS/ATL12.003

Neuenschwander, A. L., & Magruder, L. A. (2016). The potential impact of vertical sampling uncertainty on ICESat-2/ATLAS terrain and canopy height retrievals for multiple ecosystems. *Remote Sensing*, *8*(12), 1039.

Neumann, T. A., A. Brenner, D. Hancock, J. Robbins, J. Saba, K. Harbeck, A. Gibbons, J. Lee, S. B. Luthcke, T. Rebold, et al. 2020. ATLAS/ICESat-2 L2A Global Geolocated Photon Data, Version 3. Boulder, Colorado USA. NASA National Snow and Ice Data Center Distributed Active Archive Center, https://doi.org/10.5067/ATLAS/ATL03.003

Sandwell, D. T., Müller, R. D., Smith, W. H., Garcia, E., & Francis, R. (2014). New global marine gravity model from CryoSat-2 and Jason-1 reveals buried tectonic structure. *Science*, *346*(6205), 65-67.

Sandwell, D. T., Harper, H., Tozer, B., & Smith, W. H. (2019). Gravity field recovery from geodetic altimeter missions. *Advances in Space Research*.

Savage, A. C., Arbic, B. K., Alford, M. H., Ansong, J. K., Farrar, J. T., Menemenlis, D., ... & Wallcraft, A. J. (2017). Spectral decomposition of internal gravity wave sea surface height in global models. *Journal of Geophysical Research: Oceans*, *122*(10), 7803-7821.

Schaeffer, P., M. I. Pujol, Y. , Faugere, E. Charles, A. Delepoulle, T. Sandwell, Q. Dagneaux, R. Baghi, G. Dibarbourne, and N. Picot. (2018). What do we need to improve the next Mean Sea Surface?, Ocean Surface Topography Science Team Meeting, Ponta Delgado, Portugal, September, 2018.

Smith, B., Fricker, H. A., Gardner, A. S., Medley, B., Nilsson, J., Paolo, F. S., ... & Harbeck, K. (2020). Pervasive ice sheet mass loss reflects competing ocean and atmosphere processes. *Science*, 368(6496), 1239-1242.

Stopa, J. E. (2019). Seasonality of wind speeds and wave heights from 30 years of satellite altimetry. *Advances in Space Research*.

Sverdrup, H. U., & Munk, W. H. (1947). *Wind, sea and swell: Theory of relations for forecasting* (No. 303). Hydrographic Office.

Tchilibou, M., Gourdeau, L., Morrow, R., Serazin, G., Djath, B., & Lyard, F. (2018). Spectral signatures of the tropical Pacific dynamics from model and altimetry: a focus on the meso-/submesoscale range. *Ocean Science*, *14*(5), 1283-1301.

Villas Bôas, A. B., Gille, S. T., Mazloff, M. R., & Cornuelle, B. D. (2017). Characterization of the deep water surface wave variability in the California Current region. *Journal of Geophysical Research: Oceans*, *122*(11), 8753-8769.

Wessel, P., Smith, W. H., Scharroo, R., Luis, J., & Wobbe, F. (2013). Generic mapping tools: improved version released. *Eos, Transactions American Geophysical Union*, /94/(45), 409-410.

Xu, Y., & Fu, L. L. (2012). The effects of altimeter instrument noise on the estimation of the wavenumber spectrum of sea surface height. *Journal of Physical Oceanography*, *42*(12), 2229-2233.

Yale, M. M., Sandwell, D. T., & Smith, W. H. (1995). Comparison of along-track resolution of stacked Geosat, ERS 1, and TOPEX satellite altimeters. *Journal of Geophysical Research: Solid Earth*, *100*(B8), 15117-15127.

Young, I. R. (1999). *Wind generated ocean waves*. Elsevier.

Zhang, S., & Sandwell, D. T. (2017). Retracking of SARAL/AltiKa radar altimetry waveforms for optimal gravity field recovery. *Marine Geodesy*, *40*(1), 40-56.